Journal of Applied Geophysics 131 (2016) 41–53

Contents lists available at ScienceDirect

Journal of Applied Geophysics

journal homepage: www.elsevier.com/locate/jappgeo

Numerical modeling of seismic waves using frequency-adaptive meshes

Jinyin Hu, Xiaofeng Jia *

Laboratory of Seismology and Physics of Earth's Interior, School of Earth and Space Sciences, University of Science and Technology of China, 96 Jinzhai Rd., Hefei, Anhui 230026, China

ARTICLE INFO

Article history:
Received 9 September 2015
Received in revised form 29 April 2016
Accepted 24 May 2016
Available online 25 May 2016

Keywords:
Frequency-adaptive
Numerical modeling
Wave propagation
Propagation angle

ABSTRACT

An improved modeling algorithm using frequency-adaptive meshes is applied to meet the computational requirements of all seismic frequency components. It automatically adopts coarse meshes for low-frequency computations and fine meshes for high-frequency computations. The grid intervals are adaptively calculated based on a smooth inversely proportional function of grid size with respect to the frequency. In regular grid-based methods, the uniform mesh or non-uniform mesh is used for frequency-domain wave propagators and it is fixed for all frequencies. A too coarse mesh results in inaccurate high-frequency wavefields and unacceptable numerical dispersion; on the other hand, an overly fine mesh may cause storage and computational overburdens as well as invalid propagation angles of low-frequency wavefields. Experiments on the Padé generalized screen propagator indicate that the Adaptive mesh effectively solves these drawbacks of regular fixed-mesh methods, thus accurately computing the wavefield and its propagation angle in a wide frequency band. Several synthetic examples also demonstrate its feasibility for seismic modeling and migration.

1. Introduction

Seismic wave modeling is an important tool for understanding complex wave phenomena in realistic heterogeneous media. It typically includes two key steps: discretizing the model with grid-based schemes and solving the wave equation. For the latter, the frequency-domain wave propagator is one of the widely used methods in seismic modeling and it is of special interest in many applications, such as multisource experiments (Pratt and Worthington, 1990), the frequency-domain acoustic-wave modeling (Operto et al., 2007; Moreira et al., 2014), the frequency-domain elastic-wave modeling (Gosselin-Cliche and Giroux, 2014; Li et al., 2015) and the frequency-domain seismic in vertical transversely isotropic media (Operto et al., 2014). The choice of wave propagators directly determines the computational efficiency and accuracy of modeling. Furthermore, the grid interval is a key factor that affects modeling accuracy and efficiency as long as the numerical algorithm is based on grid discretization, such as in the finite difference method (e.g., Shan, 2009; Martin et al., 2015) and the finite element method (e.g., Wang et al., 2013; Ansari and Farquharson, 2014). A too coarse discretization (undersampling) results in inaccurate solutions and unacceptable numerical dispersion, while an overly fine discretization (oversampling) may cause storage and computational overburdens (Falk et al., 1998; Tessmer, 2000). This dilemma occurs especially when the medium is quite heterogeneous and uniform grids are used for discretization. Moreover, a uniform grid may lead to large errors near the source point when a finite difference scheme is applied for solving the eikonal equation (Vidale, 1988; Qin et al., 1992; Kim and Cook, 1999; Qian and Symes, 2002; Zhao, 2005; Qian et al., 2007; Sun et al., 2011). For these reasons, it is crucial in modeling to define an appropriate discrete grid.

To balance the accuracy and efficiency of seismic modeling in complex media, grid-based methods with improvements are proposed, such as the finite-difference method using staggered grids (Chu and Stoffa, 2011; Wang et al., 2014; Ren and Liu, 2015), rotated staggered grids (Saenger et al., 2000; Krüger et al., 2005; Bohlen and Saenger, 2006; Bansal and Sen, 2008), mixed-grids (Hustedt et al., 2004), variable time steps (Tessmer, 2000) and adaptive variable-length spatial operators (Liu and Sen, 2011a, 2011b). They are mostly dependent on uniform grid mesh. Space-adaptive grid schemes are proposed in which the model is discretized with a spatially non-uniform grid mesh. Those employ irregular grids (Moczo, 1989; Jastram and Behle, 1992; Jastram and Tessmer, 1994; Opršal and Zahradník, 1999; Adriano and Oliveira, 2003), variable grids (Wang and Schuster, 1996; Hayashi and Burns, 1999), or discontinuous grids (Aoi and Fujiwara, 1999). The common point of these methods is basically to adopt fine grids in low-velocity regions or small-scale structures and coarse grids in high-velocity regions or large-scale structures. These space-adaptive meshes are also employed to handle the topography of the computational area (Zhang and Chen, 2006), or to improve the stability and accuracy of the finite difference solution to the eikonal equation along the expanding wavefront (Sun et al., 2007). In general they improve accuracy with minimal increase in computational cost. However, varying the grid interval may give rise to artificial reflections and therefore should be employed with care.

* Corresponding author.
E-mail address: xjia@ustc.edu.cn (X. Jia).

http://dx.doi.org/10.1016/j.jappgeo.2016.05.011
0926-9851/

The space-adaptive mesh mentioned above is, in fact, velocity-adaptive and wavelength-adaptive. In this way, the grid interval coincides well with the wavelength to keep the algorithm stable and accurate without much dispersion. Note that the wavelength is dependent on the frequency as well as the velocity. Naturally, it is also effective to vary the grid interval with the frequency instead of the velocity. Compared with the velocity- or space-adaptive mesh, the frequency-adaptive mesh can be applied to frequency-domain wave propagators easily (e.g., Fichtner et al., 2013; Li et al., 2015). In space-adaptive approaches, the grid mesh is determined by the wavelength of the highest-frequency wavefield to ensure the mesh is appropriate for all frequencies wavefields, or undersampling may corrupt the result of the wavefield simulation due to the numerical dispersion. However, such a very fine mesh unavoidably increases the computational cost especially in 3D cases. On the other hand, the wave propagation angle for lower frequencies, one of the key parameters in seismic processing, cannot be computed accurately using the highest frequency-based mesh.

The propagation angle is generally calculated by ray tracing, in which the slowness vector denotes the propagation direction of the wavefront (Aki and Richards, 1980; Cerveny, 2001; Bruneton et al., 2002; Gray, 2006; Ruud, 2006). However, the ray-based method is difficult to apply with frequency-domain wave propagators such as the Padé generalized screen propagator (GSP) (Xie and Wu, 1998) due to its frequency limitation. Jia and Wu (2009a) presented an alternative method that makes use of the wavefield gradient to obtain the wave propagation angle. Based on their results, in the low-frequency case, the wave propagation angle is likely calculated within the scale of less than one wavelength and thus yields invalid results. In brief, the calculation of the wavefield and its propagation angle in a wide frequency band poses issues for frequency-domain wave propagators based on a single and fixed mesh.

In this paper, we apply an algorithm using frequency-adaptive meshes for seismic modeling and migration. The model is discretized with different uniform grid meshes for different frequency wave components. Grid meshes are coarse for low-frequency computations and relatively fine for high-frequency computations. Grid meshes coincide with frequencies. The grid size and the grid interval are adaptively calculated based on the corresponding frequency. Compared with regular fixed-mesh methods, this method is more suitable for frequency analysis and multi-scale study and accurately calculates the wavefield and the wave propagation angle in a wide frequency band. In this study, we employ GSP (Le Rousseau and de Hoop, 2001a, 2001b; Chen, 2010; Shin et al., 2015), a standard frequency-domain propagator, to test the adaptive-mesh method. Without modification to the propagator, this approach can be applied to other frequency-domain wave propagators.

The theory and methods of the frequency-adaptive mesh are addressed in the next section. We first introduce the theory of frequency-adaptive mesh and develop it for the GSP method. Then, we discuss the advantage of this approach for computing propagation angles in frequency-domain and analyze its numerical dispersion. The third section presents two synthetic tests to compare modeling results and migration results of the adaptive-mesh GSP method with the fixed-mesh GSP method. The conclusion is drawn in the final section.

2. Theory and methods

An algorithm that uses frequency-adaptive meshes is proposed to try to satisfy the computational requirements of different frequencies, in which the computational area is discretized with different uniform grid meshes for different frequency wave components. More specifically, it automatically adopts coarse meshes for low-frequency computations and fine meshes for high-frequency computations. The grid intervals are adaptively calculated based on a function between the grid interval (denoted by h) and the frequency (denoted by ω). Therefore, defining an appropriate relationship function $h(\omega)$ is a crucial part of this method. In principle, any function may be used for $h(\omega)$ as long as the grid meshes are coarse for low frequencies and fine for high frequencies. However, the numerical dispersion must be taken into account when stacking the frequency wave components into the time domain. Therefore, the $h(\omega)$ curve should be defined to satisfy numerical dispersion. Additionally, the computational efficiency, numerical stability and possible artifacts should also be considered when defining $h(\omega)$.

For a reasonable $h(\omega)$, different grid meshes are applied for different frequency components as Fig. 1 shows. During the computation of each frequency component, the input original velocity model is interpolated into the corresponding grid. The computing results, that is the single-frequency wavefield, will be interpolated into a common grid (mesh(*out*) shown in Fig. 1) to stack back into the time domain and output the final result. To interpolate the input velocity and single-frequency-wavefields, classic linear, quadratic or spline interpolation can be adopted in our method; other approaches such as the interpolation scheme using Kaiser windowed sinc functions (Hicks, 2002) may also be employed for high accuracy. In this paper, we used the linear interpolation due to its less time–cost. Additionally, the spatial fitting of grids and source positions must be considered during interpolations. To do this, during interpolation we fix the source location on a grid point as the starting point (shown by the red point in Fig. 2), and interpolate the velocity from the starting point to the sides successively. This process confirms that the absolute source location is correct. For seismic modeling these interpolations mentioned above are necessary. For seismic migration, the workflow is plotted in Fig. 3 and it is necessary to perform an extra interpolation on seismic data. We resample the data by interpolation to guarantee the fit of the grid and the receivers' positions. Given that the time-distance curve of reflection waves is usually a quadratic function, we apply the quadratic interpolation and the state-of-the-art interpolation or data regularization approaches (Hicks, 2002; Jin, 2010) can also be used here.

2.1. GSP method with frequency-adaptive meshes

The implementation of adaptive meshes is completely independent of the wave propagator itself. We propose a discretization strategy for all grid-based frequency-domain propagators. In this paper, as an example, we develop the theory of frequency-adaptive meshes for the GSP method. GSP is a typical frequency-domain propagator and the wavefield has the form of (Appendix A)

$$u(x,z_1)=\left(\mathrm{F}^{-1}-i\Delta z k_0 A\mathrm{F}^{-1}\frac{k_x^2}{k_0^2}\right)e^{i\Delta z k_z}\mathrm{F}e^{-i\Delta z k_0\frac{\delta v(x,z_0)}{v(x,z_0)}}u(x,z_0), \tag{1}$$

where $u(x,z_1)$ is the pressure component, $z_1=z_0+\Delta z$ and Δz is the depth step, $\delta v(x,z_0)/v(x,z_0)$ stands for the relative velocity perturbation, k_0, k_x and $k_z=\sqrt{k_0^2+k_x^2}$ are the background, transverse and vertical wavenumber, respectively; i is the imaginary unit, F refers to Fourier transform from the space domain to the wavenumber domain and $A=(1/2)\{[1/(v_0/v(x,z_0))*]-1\}$ in which v_0 is a reference velocity, $[1/(v_0/v(x,z_0))*]$ is the Fourier transform of $1/(v_0/v(x,z_0))$ and "*" denotes the convolution in wavenumber domain. Based on Appendix A, the GSP can be given totally in the wavenumber domain by

$$u(k_x,z_1)=\exp\left[i\Delta z k_z-i\Delta z k_0\left(\frac{\delta v(x,z_0)}{v(x,z_0)}*\right)-i\Delta z k_0 A\frac{k_x^2}{k_0^2}\right]u(k_x,z_0). \tag{2}$$

On the right hand side of Eq. (2), the first two terms refer to the phase screen solution; the third term is the modification for perturbations of large velocities and large angles. In this research, the frequency-adaptive meshes algorithm primarily addresses two critical numerical artifacts produced by fixed-grids pacing. The first is the wave propagation angle anomalies produced by fine grid for low-frequency components. The

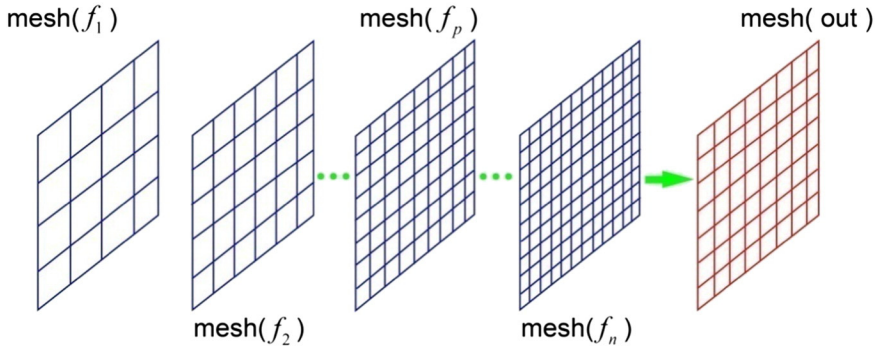

Fig. 1. Illustration of meshes for different frequency components. $f_1 \sim f_n$ denote the frequency varying from small to large, and f_p is the dominant frequency. 'mesh(*out*)' is the common mesh for stacking wave components.

second includes the numerical dispersion due to insufficient sampling for high-frequency components.

2.2. Calculation of the wave propagation angle

The wave propagation angle, a key factor in seismic processing (Sava and Fomel, 2003; Ursin et al., 2005; Jia and Wu, 2009a; Sun et al., 2010), is one of the concerns of frequency-adaptive mesh theory as mentioned above. The propagation angle obtained by ray tracing is based on high-frequency approximations and can hardly be used by low and modest frequencies. Therefore, for frequency-domain propagators we have to apply other methods to calculate the propagation angle. Jia and Wu (2009a) proposed a useful method to employ the wavefield gradient to calculate the propagation angle. It is especially effective for dual-domain propagators (e.g. GSP) since the wavefield gradient can be easily obtained in space-frequency domain. Compared with the notable approach using Poynting vector (Dickens and Winbow, 2011) to represent the propagating direction, this approach takes less cost and is more easily implemented (especially in the frequency domain). In acoustic cases the wavefield gradient and Poynting vector have the same direction. Here we adopt Jia and Wu's method to calculate the propagation angle and derive the wavefield gradient directly from the marching expression of GSP. According to Eq. (1), we have the horizontal component of the wavefield gradient as

$$\frac{\partial u(x,z_1)}{\partial x} = i\left(\mathrm{F}^{-1} - i\Delta z k_0 A \mathrm{F}^{-1}\frac{k_x^2}{k_0^2}\right) k_x e^{i\Delta z k_z} \mathrm{F} e^{-i\Delta z k_0 \frac{\delta v(x,z_0)}{v(x,z_0)}} u(x,z_0). \tag{3}$$

Based on the other form of GSP given by Eq. (2), we have its unintegrated form as

$$\frac{\partial u(k_x,z)}{\partial z} = i\left[k_z - k_0\left(\frac{\delta v(x,z_0)}{v(x,z_0)}*\right) - k_0 A\frac{k_x^2}{k_0^2}\right] u(k_x,z). \tag{4}$$

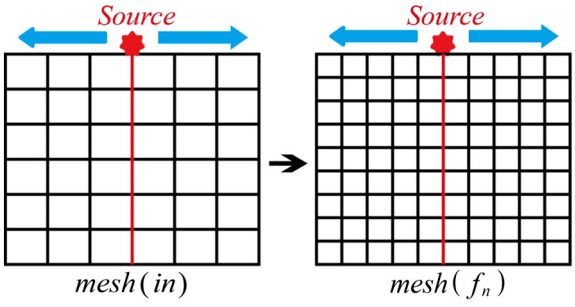

Fig. 2. Illustration of interpolating velocity model. (For interpretation of the references to color in this figure, the reader is referred to the web version of this article.)

From Eq. (4), the vertical component of the wavefield gradient is given as

$$\frac{\partial u(x,z_1)}{\partial z} = ik_z u(x,z_1) - ik_0\frac{\delta v(x,z_0)}{v(x,z_0)}u(x,z_1) + i\frac{A}{k_0}\frac{\partial^2 u(x,z_1)}{\partial x^2}. \tag{5}$$

Actually, a finite-difference of the quantities $\partial u(x,z_1)/\partial x$ and $\partial u(x,z_1)/\partial z$ from the wavefield $u(x,z_1)$ is simpler and less time-consuming than Eqs. (3) and (5). However, we use Eqs. (3) and (5) due to their higher accuracy. Once the gradient vector is obtained, we have the wave propagation angle with respect to the vertical direction as

$$\theta(x,z) = \tan^{-1}\left(\left|\frac{\partial u(x,z)}{\partial x}\right| \Big/ \left|\frac{\partial u(x,z)}{\partial z}\right|\right). \tag{6}$$

For dual-domain wave propagators such as GSP, the wavefield values are usually complex. Therefore, absolute values are used in Eq. (6).

However, note that the wavefield gradient has no explicit physical meaning. It only indicates the variation of wavefield values between two spatial points and doesn't naturally represent the direction of the wave propagation. The key reason is that the basic unit in seismic energy (i.e. group) propagation is a wavelet package. Therefore, when measuring the flowing direction of seismic energy, one wavelet package should be considered as a single unit. This principle must be followed when calculating the wavefield gradient and avoids processing it within one wavelet package. Fig. 4 provides a conceptual illustration of using the same grid to calculate the wavefield gradient for two different frequency components. Note that the shown wavefields are computed

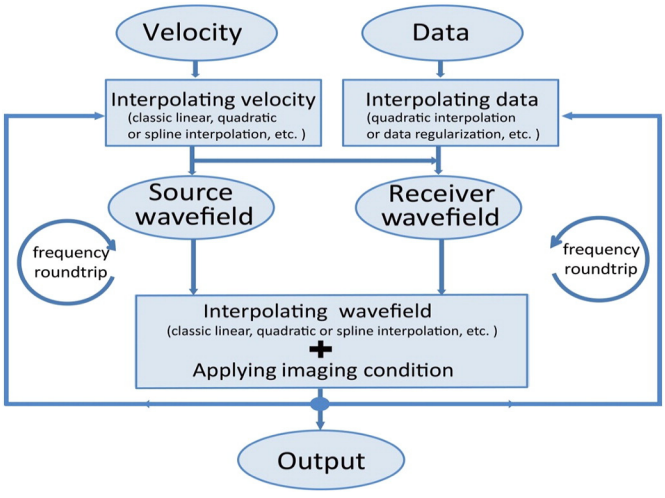

Fig. 3. The migration workflow of the method with frequency-adaptive meshes.

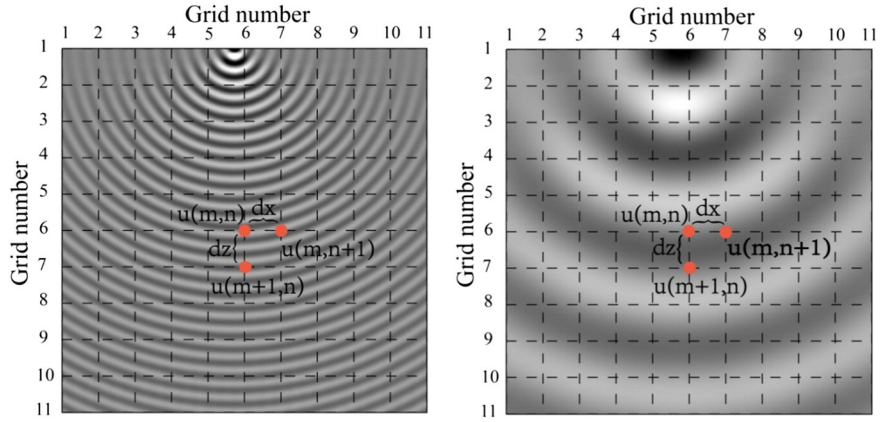

Fig. 4. Conceptual illustration of calculating wavefield gradients for different frequency wave components on a common mesh. The dashed lines refer to grid lines. $u(m,n)$, $u(m+1,n)$ and $u(m,n+1)$ denote the wavefields at grid points (m,n), $(m+1,n)$ and $(m,n+1)$, respectively. dx is the horizontal grid interval and $dz$the vertical. (a) For a high-frequency wave component, the grid interval is either greater than the wavelength or has the same scale. (b) For a low-frequency wave component, the grid interval is less than the wavelength.

not exactly by the plotted grid. Based on the above analysis, the spatial distance between $u(m,n)$, $u(m+1,n)$ and $u(m,n+1)$ in Fig. 4 should be larger than one wavelength or at least shouldn't be less than one wave length too much. In this way the wavefield gradient can represent the direction of wave propagation. Otherwise, the x-direction component of the wavefield gradient (denoting the variation from $u(m,n)$ to $u(m,n+1)$) and z-direction component (denoting the variation from $u(m,n)$ to $u(m+1,n)$ can't indicate the seismic propagation. Fine mesh can surely provide accurate wavefield, but using the same fine mesh to calculate wavefield gradient may lead to invalid propagation direction in low frequency cases. An alternative approach is to calculate the wavefield and its gradient with different grid intervals. After obtaining accurate wavefield as shown in Fig. 4a, we skip some grid points to calculate the wavefield gradient meaning that dx, dz actually include several grid points of the original mesh. In brief, only in the case that grid interval is larger than the wavelength or have the same scale, can the wavefield gradient accurately represent the direction of wave propagation as shown in Fig. 4a and thus the propagation angle obtained by Eq. (6) is right.

For the low frequency, its wavelength is large. Hence, we need to take more attentions into processing wavefield gradient. In regular frequency-domain algorithms, the model is discretized with uniform or non-uniform meshes. The grid interval is determined by the shortest wavelength and fixed for calculating all single-frequency wave components so that in the case of very low frequency computation, the wavelength is larger than the grid interval and thus the computation of wavefield gradient is processed in the scale of less than one wavelength (Fig. 4b). In this way, the wavefield gradient obtained from Eqs. (3) and (5) is inaccurate and fails to represent the true direction of seismic energy flow. By solving Eq. (6), this anomaly of the direction vector will be evident in the distribution of propagation angle for a single frequency and then corrupt results of propagation-angle-based methods such as the superwide-angle wave propagator (Jia and Wu, 2009b).

In the superwide-angle wave propagator a propagation-angle-based weight function is employed to conduct wavefield reconstruction; therefore correctly computing propagation angles for all frequencies is quite important. With regular fixed mesh, the angles for low-frequencies cannot be guaranteed. Fig. 5 shows an example for BP 2004 model of using the superwide-angle migration with the fixed mesh. In this test, the minimum frequency, dominant frequency and maximum frequency for the source are 5 Hz, 27 Hz and 40 Hz respectively. The shortest wavelength with respect to minimum velocity 1500 m/s (Fig. 5c) is 37.5 m. We define a grid with $\Delta x = 12.5$ m and $\Delta z = 12.5$ m and thus 3 grid points per shortest wavelength have been used. Fig. 5a is the migration image of the superwide-angle method with this fixed mesh. The propagation angles for each frequency are computed based on corresponding wavefields so the image for each frequency is computed based on different angle-based weight functions. Based on the discussions above the weight functions of low frequencies may be incorrect. For this reason, the images corresponding to different frequencies can hardly coincide with one another so that the stack image appears smeared. As two red arrows show, Fig. 5a has some noise, and the resolution is not high enough at the salt boundary. In this case, the high frequency's propagation angles are computed correctly. For comparison, we chose the propagation angle of the frequency 83 Hz to calculate the weight function for all frequencies. As Fig. 5b shows, the migration image of the salt has clearly been improved especially in areas indicated by two red arrows. To ensure the accuracy of propagation angles, the propagation angle of the high frequency can be saved and adopted by all frequency components. Additionally, the frequency-adaptive mesh will also be a useful scheme, in which the model is discretized with different uniform meshes for the computations of different frequency components and the mesh size is determined by the corresponding minimum wavelength.

2.3. Numerical dispersion analysis

Numerical dispersion poses a significant problem for most numerical algorithms and a great deal of the literature examines this topic (e.g., Alford et al., 1974; Dablain, 1986; Brzostowski and Black, 1989). The grid interval needs to be finer than that determined by sampling theorem. In this section we discuss the numerical dispersion of frequency-adaptive meshes.

First, we take the finite difference as an example. The 2D acoustic wave equation is given by

$$\frac{1}{v(x,z)^2}\frac{\partial^2 u(x,z)}{\partial t^2} = \frac{\partial^2 u(x,z)}{\partial x^2} + \frac{\partial^2 u(x,z)}{\partial z^2}, \tag{7}$$

where $u(x,z)$ is the pressure and v is the velocity of seismic wave without dispersion. Its 2N-order finite-difference solution based on square grids is given by Fan et al. (2015)

$$\begin{aligned}\frac{1}{v(x,z)^2}\frac{\partial^2 u(x,z)}{\partial t^2} = {} & \frac{1}{\Delta x^2}\sum_{j=1}^{N} w_j^{(N)}[u(x+j\Delta x,z)-2u(x,z)+u(x-j\Delta x,z)] \\ & + \frac{1}{\Delta z^2}\sum_{j=1}^{N} w_j^{(N)}[u(x,z+j\Delta z)-2u(x,z)+u(x,z-j\Delta z)],\end{aligned} \tag{8}$$

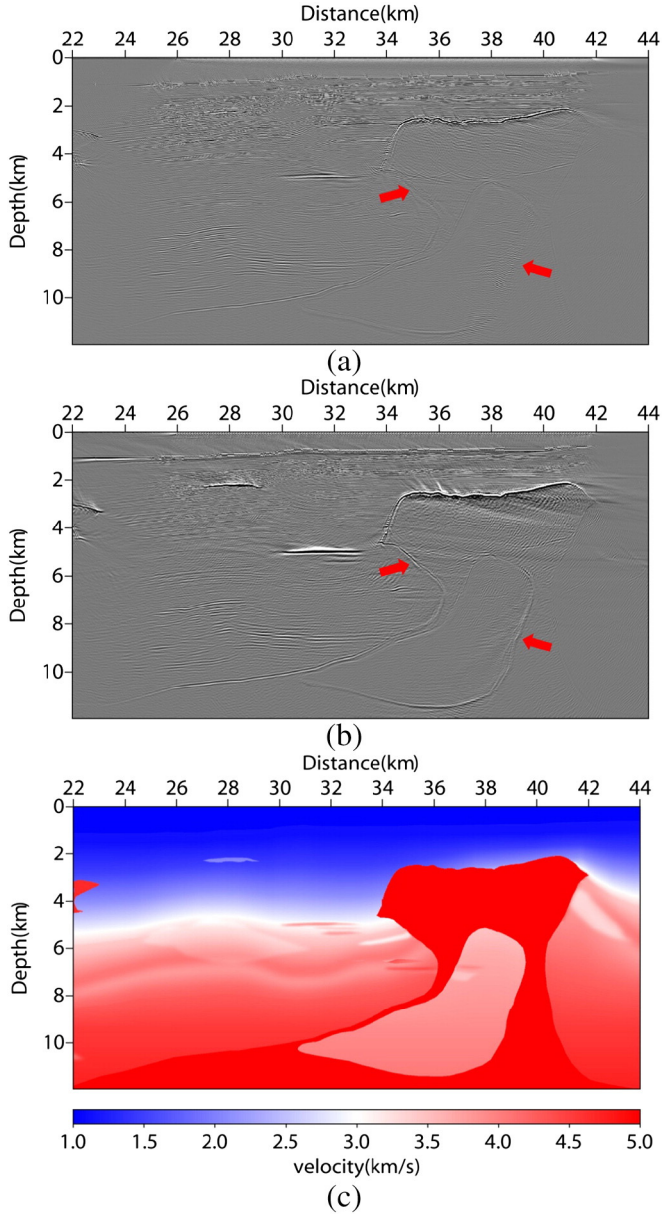

Fig. 5. The stacked images of superwide-angle migration. The angle-based weight functions for each frequency are computed by (a) corresponding wavefields and (b) the wavefield of 83 Hz, respectively. (c) The part of BP2004 model used in this case. (For interpretation of the references to color in this figure, the reader is referred to the web version of this article.)

where $w_j^{(N)}$ is the finite-difference coefficients; $\Delta x = \Delta z = h$ are the grid intervals in the x and z directions, respectively. Consider a plane harmonic wave whose wave propagation angle with respect to the z direction is α, in the form of

$$u(x,z,t) = \exp[i(\omega t - kx\sin\alpha - kz\cos\alpha)], \tag{9}$$

where k is the wavenumber. Substituting Eq. (9) into Eq. (8), we obtain the dispersion equation as follows

$$\omega^2 = \frac{-2v(x,z)^2}{h^2}\sum_{j=1}^{N} w_j^{(N)}[\cos(jkh\sin\alpha) + \cos(jkh\cos\alpha) - 2]. \tag{10}$$

Consequently, according to $\omega = k\bar{v}$ where $\bar{v}$ is the numerical dispersion velocity, we have

$$\delta^2 = \frac{-2}{(kh)^2}\sum_{j=1}^{N} w_j^{(N)}[\cos(jkh\sin\alpha) + \cos(jkh\cos\alpha) - 2], \tag{11}$$

where $\delta = \bar{v}(x,z)/v(x,z)$. For a specified frequency ω, the greater the difference between $\bar{v}(x,z)$ and $v(x,z)$, the greater the dispersion. If $\delta = 1$, there is no numerical dispersion. In the fixed-mesh method the grid intervals employed for all single-frequency computations are the same, and then hk is related to frequency and gets its maximum value π at the Nyquist frequency. Therefore, δ is also frequency-dependent, and this is one factor that accounts for the dispersion. Fig. 6 plots the dispersion curves in the homogeneous medium (3 km/s) for $h = 10$ m, 15 m, 20 m and 30 m, respectively. As the frequency increases, δ drops quickly from 1 meaning great dispersions occur because the grids are not fine enough. In our method, the grid interval is the function of frequency, and the dispersion equation is modified as

$$\delta^2 = \frac{-2}{[kh(\omega)]^2}\sum_{j=1}^{N} w_j^{(N)}[\cos(jkh(\omega)\sin\alpha) + \cos(jkh(\omega)\cos\alpha) - 2], \tag{12}$$

where $h(\omega)$ is the function between the grid interval and frequency. In this case, it may be possible to make δ independent of ω by defining an appropriate $h(\omega)$, and we believe this will be helpful to suppress the dispersion. Considering there is a linear relationship between k and ω, we primarily investigate the inversely proportional function defined by sampling theorem. It is given by

$$h(\omega) = \lambda_{\min}(\omega)/n, i.e.\ \ h(\omega) = (2\pi \times v_{\min}/\omega)/n \tag{13}$$

where $\lambda_{\min}(\omega)$ is the minimum wavelength of corresponding frequency; n is the number of sampling points within $\lambda_{\min}(\omega)$ and $v_{\min}$ is the minimum velocity. Consequently, hk is not a function of the frequency; thus, δ is independent of the frequency. As the red line in Fig. 6 shows, the dispersion error δ of our approach with the grid variation function $h(\omega) = \lambda(\omega)/10$ is always close to 1, while other four grids cause large numerical dispersion as the frequency increases since their grid intervals do not satisfy the requirement for the 4-order finite difference modeling (i.e., five or more grid points per minimum wavelength). Moreover, to suppress dispersion the inversely proportional function $h(\omega)$ must be smooth because an unsmooth $h(\omega)$ indicates that hk is still a function of the frequency and may give rise to great dispersion.

The above discussion is based on the finite difference solution of the wave equation. Similarly, we can obtain the dispersion equation for

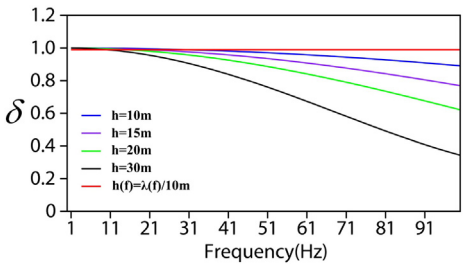

Fig. 6. Dispersion curves of the spatial 4-order 2D finite-difference method. The velocity is 3 km/s, the frequency band is 1 Hz–100 Hz and the propagation angle is 30°. For grid intervals of 10 m, 15 m, 20 m and 30 m, the number of grid point per minimum wavelength are 3, 2, 1.5 and 1 respectively. The minimum grid interval from the grid variation function $h(f) = \lambda(f)/10$ is 3 m and the maximum one is 300 m. (For interpretation of the references to color in this figure, the reader is referred to the web version of this article.)

fixed-mesh GSP method as follows

$$\exp(-ikz_1\cos\alpha) = \exp\left\{i\left[hk_0\cos\alpha - hk_0\left(\frac{\delta v(x,z_0)}{v(x,z_0)}*\right) - hk_0A\sin^2\alpha\right]\right\}\exp(-ikz_0\cos\alpha), \quad (14)$$

where $(\delta v(x,z_0)/v(x,z_0)*)$ is the Fourier transform of $\delta v(x,z_0)/v(x,z_0)$, "*" denotes the convolution in wavenumber domain, and the dispersion equation for adaptive-mesh GSP method can be expressed as

$$\exp(-ikz_1\cos\alpha) = \exp\left\{i\left[h(\omega)k_0\cos\alpha - h(\omega)k_0\left(\frac{\delta v(x,z_0)}{v(x,z_0)}*\right) - h(\omega)k_0A\sin^2\alpha\right]\right\} \times \exp(-ikz_0\cos\alpha). \quad (15)$$

In the GSP method with frequency-adaptive meshes, it is almost impossible to generate an explicit expression of the numerical dispersion error δ and quite difficult to define one appropriate $h(\omega)$ directly from Eq. (15). However, the derivation of GSP includes no frequency approximations so the above conclusion for FD is also valid for GSP. To verify it, in the following experiments, we study several possible $h(\omega)$ functions for a simple model and choose the best one for further modeling and migration.

3. Numerical experiments

3.1. Numerical modeling experiments

First, we apply GSP to compute wavefields for frequencies of 10 Hz and 50 Hz respectively. The same mesh of grid interval 10 m is used. The velocity is 2 km/s, so the wavelength of 50 Hz is 40 m and there are 4 grid points per wavelength. However it is still not enough for the 50 Hz component. As expected, the wavefield at 50 Hz contains strong numerical dispersion as Fig. 7b shows, while this mesh performs well for the low frequency of 10 Hz (Fig. 7a). To avoid undersampling for the high frequency of 50 Hz, the mesh has to be finer enough. In regular methods, the grid interval determined by the maximum frequency is used for all frequencies components to guarantee wavefields accurate enough. Using such a fine grid will dramatically increase the computational time and memory storage especially in 3D cases. It is actually unnecessary for computations at low frequencies.

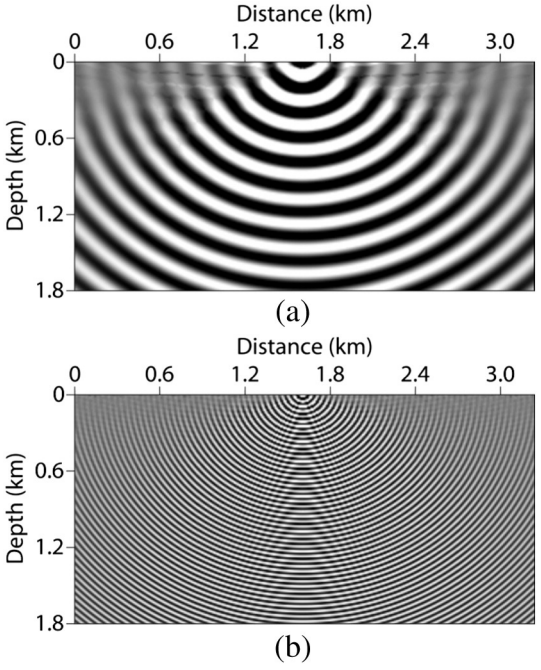

Fig. 7. Single-frequency wavefields in a constant velocity (2 km/s) model. The source is located at the surface centre. The grid interval is 12 m. (a) 10 Hz; (b) 50 Hz.

On the other hand, a coarse mesh is also required to obtain accurate wave propagation angles. As shown in Fig. 8a and b, 'knotted' anomalies exist in the results of the propagation angle for low-frequency components. The anomalies disappear as the frequency increases. In the case of low frequency, the grid interval is much smaller than one wavelength, and the wavefield gradient will be processed within the scale of less than one wavelength as Fig. 4b shows. As a consequence, the wavefield gradient cannot represent the real propagated direction and thus produces invalid results. For comparison, Fig. 8e shows the angle distribution obtained by ray tracing. We see the propagation angle for high frequencies agrees well with the result of ray tracing. The differences between Fig. 8d and e are within the scale of 10^{-4} to 10^{-3} as Fig. 8f shows. We also demonstrate in Fig. 9 the distribution of ray parameter calculated with different grid intervals, varying from 5 m to 600 m for a given frequency. The denser meshes result in some 'knotted' anomalies (Fig. 9a and b). Fig. 9d illustrates that a coarse mesh is required to obtain accurate wave propagation angles.

According to the analysis above, the single and fixed mesh used in the regular GSP method is too coarse to compute high-frequency wavefields correctly, but too fine to generate accurate results on wave propagation angles for low frequencies due to conducting the first-order derivative of the wavefield. Therefore, when we need both the wavefield and its propagation angle in a wide frequency band, the regular single-mesh GSP method includes a trade-off. Fortunately, the adaptive meshes algorithm presented here can address this problem.

Unlike the space-adaptive mesh grid, which is essentially a non-uniform mesh grid, here we use uniform meshes with the grid interval h adaptively varying with frequency ω. We examine various $h(\omega)$ curves for comparison and determine the best variation function $h(\omega)$. In this example of the constant-velocity (2 km/s) model, we test the linear $h(\omega)$ curve, exponential $h(\omega)$ curve, parabolic $h(\omega)$ curve and the piecewise constant $h(\omega)$ curve and compare them with two inversely proportional $h(\omega)$ curves defined by Eq. (13). They are plotted in Fig. 10. The other four curves are designed by considering two inversely proportional curves. There are almost no intersections between the six curves except at the end points, so we can easily examine the influence of grid interval and mesh variation. Fig. 11 shows the snapshots obtained by the adaptive-mesh GSP method using these $h(\omega)$ curves shown in Fig. 10, respectively. Numerical experiments indicate that two inversely proportional $h(\omega)$ functions (red and magenta lines in Fig. 10) satisfy most of the requirements mentioned above and generate the best modeling results among the six.

Note that most grid intervals computed by the two inversely proportional curves in Fig. 10 are smaller than those computed by the linear, exponential and parabolic curves. This may explain why the inversely proportional functions provide relatively high-quality modeling results. In addition, we test the inversely proportional $h(\omega)$ curve with different n in Eq. (13). Fig. 12 shows the snapshots obtained by the adaptive-mesh GSP method using $h(\omega) = (2\pi \times v_{\min}/\omega)/n$ with $n = 3, 4, 5, 6, 7$ and 10, respectively. Numerical experiments indicate that when $n \geq 7$ the inversely proportional $h(\omega)$ functions satisfy most of the requirements mentioned above and generate the desired modeling results. Additionally, as discussed in Section *2.3 Numerical dispersion analysis*, the other requirement for $h(\omega)$ is its smoothness; strong variation of grid intervals with frequency may give rise to numerical dispersion. In Fig. 10, we see that the piecewise function provides a mesh grid even finer than the inversely proportional function with $n = 10$. However, it yields much stronger dispersion in the snapshots compared in Fig. 11d and e. This dispersion is caused by unsmooth variation of grid intervals with frequency, not by interpolations. In this method, the finer the mesh, the more interpolations it has to perform. But these

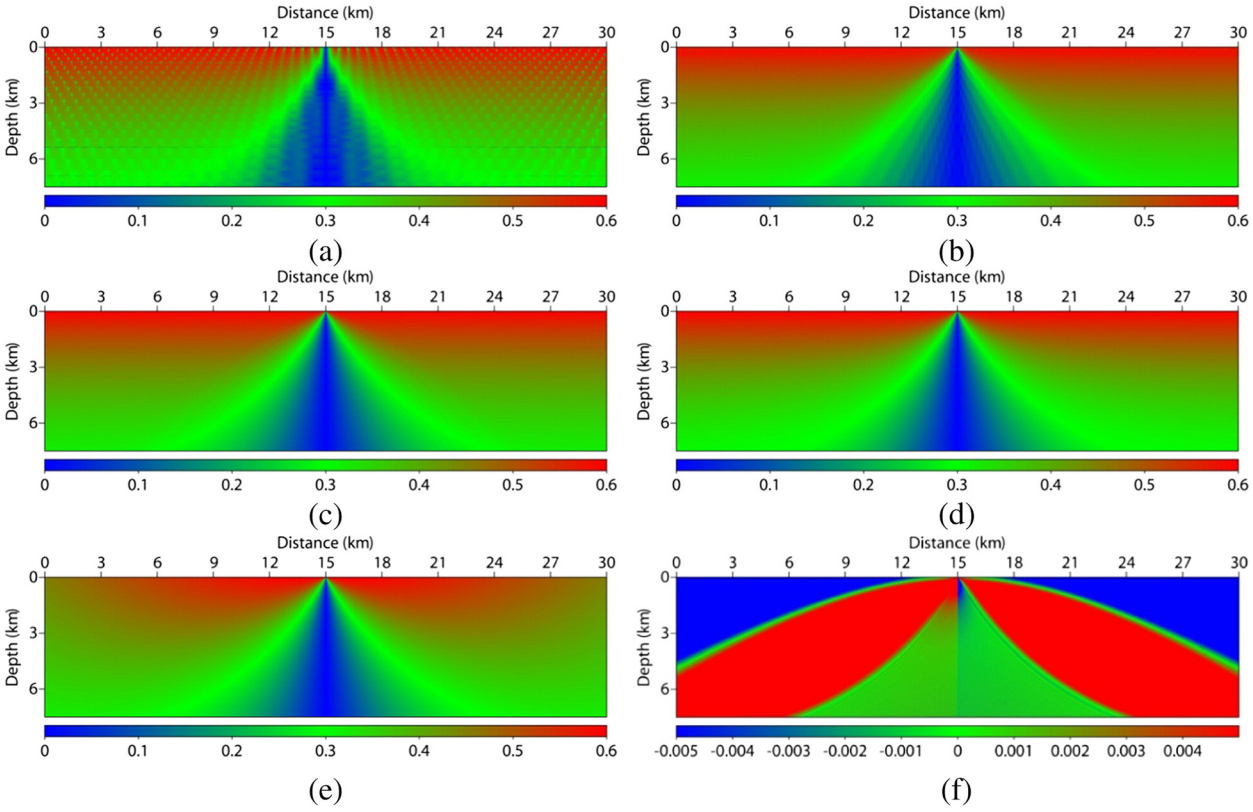

Fig. 8. Distributions of ray parameters in the medium where v(z) = 2 + 0.27z (km/s). The source is located at the surface centre. The grid interval is 10 m. For (a) ~ (d) the frequencies are 2 Hz, 10 Hz, 50 Hz and 200 Hz, respectively, and GSP is used; (e) The ray parameter provided by ray tracing; (f) The differences between (d) and (e).

interpolations do not significantly influence the numerical dispersion. For example, the magenta curve in Fig. 10 has smaller grid intervals than the other five, but it still generates the best modeling result as shown in Fig. 11f.

3.2. Migration experiments

In this section, two examples are shown to test the validity of the adaptive-mesh GSP migration and compare it with the conventional fixed-mesh GSP migration. We interpolate traces of shot gathers with a quadratic function to move receivers to the surface grid points and choose the inversely proportional function as the mesh variation function given by

$$h(\omega) = (2\pi \times v_{\min}/\omega)/10. \tag{16}$$

The interval between two adjacent frequencies is determined by $d\omega = 2\pi/(ntfft \times dt)$ where $ntfft$ is the length of Fourier transforms and dt is the time sampling interval. It is small enough so that $h(\omega)$ as defined in Eq. (16) could be regarded as a smooth curve.

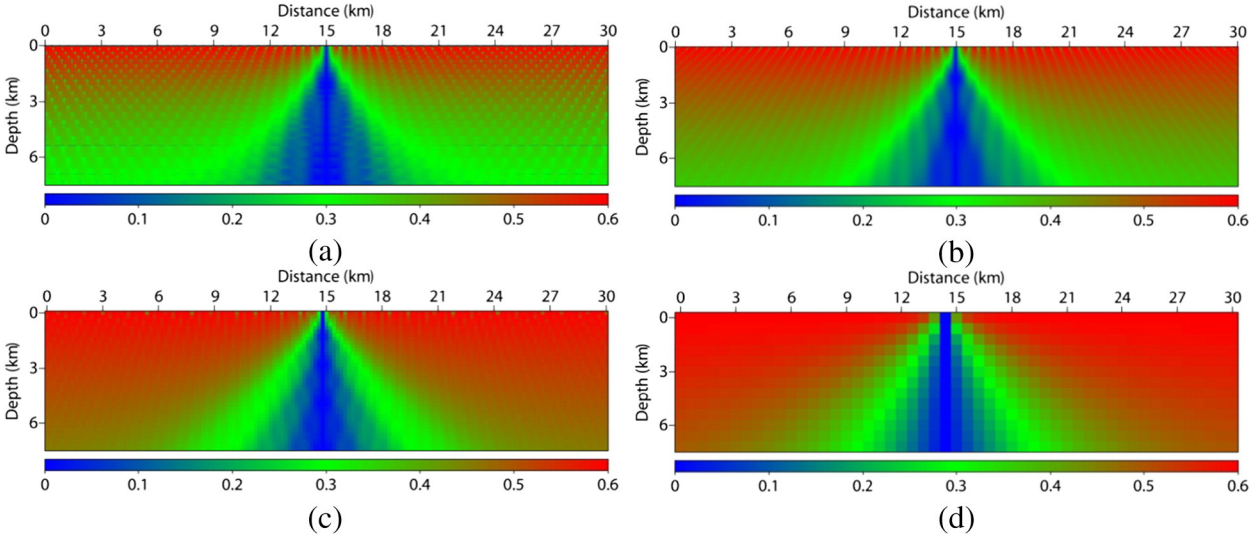

Fig. 9. Distributions of ray parameters in the medium where v(z) = 2 + 0.27z (km/s). The source is located at the surface centre. The frequency is 2 Hz. The grid intervals for (a) ~ (d) are 10 m, 50 m, 200 m and 600 m, respectively.

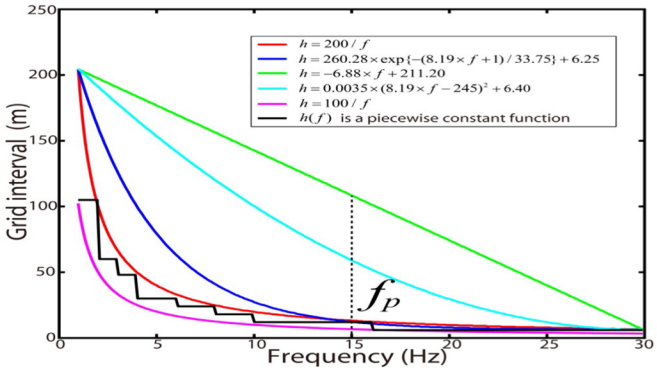

Fig. 10. Curves of the grid interval varying with frequency. (For interpretation of the references to color in this figure, the reader is referred to the web version of this article.)

The first example is a three-layer model shown in Fig. 13a. The length of the model is 7437 m and the depth is 2987 m. The mesh of 1191 × 479 grids with the grid interval $dx = dz = 6.25$ m is used to discretize the model. The synthetic data were generated by the finite difference method with 8th order spatial accuracy and 2nd order temporal accuracy. The source is a Ricker wavelet with a dominant frequency of 25 Hz, a time shift of 0.05 s, and a record length of 3 s. The receivers are distributed on the surface from 0 m to 7437 m with an interval of 12.5 m, and the shot interval is 375 m. 144 frequencies have been used in both GSP migrations with fixed mesh and adaptive mesh. The minimum frequency is 5 Hz and the maximum frequency is 40 Hz. For migration with adaptive mesh, as Fig. 3 shows, the interpolations among single-frequency wave components exist in both the source and the receiver wavefield simulations. Therefore, the interpolations complicate the cross-correlation imaging condition. We have two schemes for dealing with the imaging condition. The first scheme is to interpolate the single-frequency source wavefield $S(x,z;\omega)$ and receiver wavefield $G(x,z;\omega)$ respectively, before applying the imaging condition. The single-frequency image $I(x,z;\omega)$ is given by:

$$I(x,z;\omega) = [e_{11}S_{11}(x_{11},z_{11};\omega) + e_{12}S_{12}(x_{12},z_{12};\omega) + e_{21}S_{21}(x_{21},z_{21};\omega) + e_{22}S_{22}(x_{22},z_{22};\omega) + \ldots] \times [e_{11}G_{11}(x_{11},z_{11};\omega) + e_{12}G_{12}(x_{12},z_{12};\omega) + e_{21}G_{21}(x_{21},z_{21};\omega) + e_{22}G_{22}(x_{22},z_{22};\omega) + \ldots], \quad (17)$$

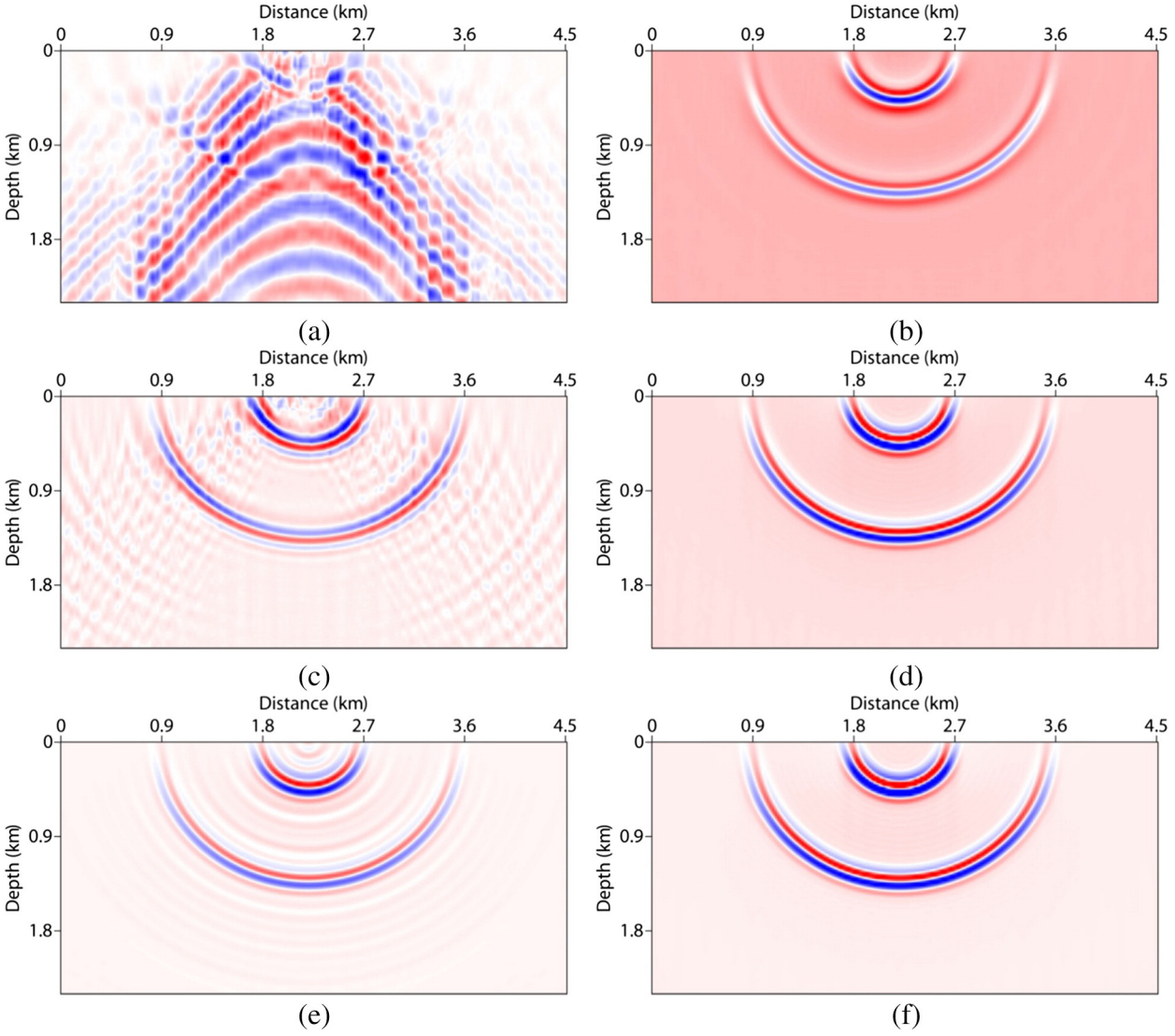

Fig. 11. Snapshots at 0.3 s and 0.75 s in a constant velocity (2 km/s) model obtained by the adaptive-mesh GSP using the different mesh variation functions shown in Fig. 10. (a) the linear curve; (b) the exponential curve; (c) the parabolic curve; (d) the red inversely proportional curve; (e) the piecewise constant function; (f) the magenta inversely proportional curve. The source is located at the surface centre. (For interpretation of the references to color in this figure legend, the reader is referred to the web version of this article.)

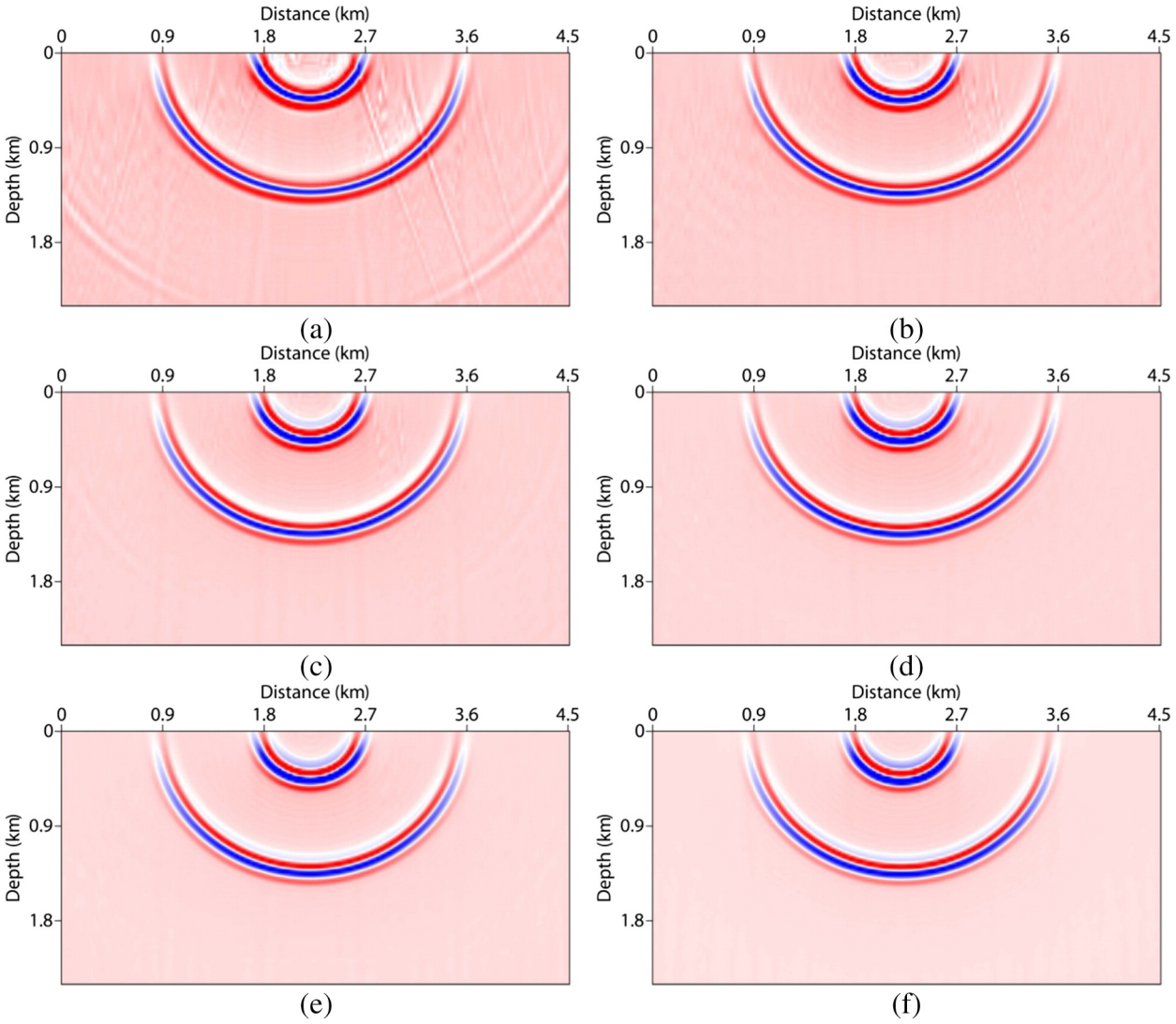

Fig. 12. Snapshots at 0.3 s and 0.75 s in a constant velocity (2 km/s) model obtained by the adaptive-mesh GSP using $h(\omega) = (2\pi \times v_{min}/\omega)/n$. (a) ~ (f) for $n = 3, 4, 5, 6, 7$ and 10, respectively. The source is located at the surface centre.

where e_{11}, e_{12}, e_{21} and e_{22} are coefficients of the 2-dimensional Lagrangian interpolation; S_{11}, S_{12}, S_{21}, S_{22} and G_{11}, G_{12}, G_{21}, G_{22} denote source wavefields and receiver wavefields on interpolation grid points, respectively. Here, the classic linear interpolation, quadratic, spline interpolation or other higher accurate interpolations can be adopted. Consequently, the image for a full frequency band is given by

$$I(x,z) = \sum_{\omega=\omega_{min}}^{\omega_{max}} I(x,z;\omega), \tag{18}$$

where ω_{min} and ω_{max} are the cut frequencies. In this test, $\omega_{min} =$ 5 Hz, $\omega_{max} = 40$ Hz. The number of frequency is 144. Fig. 13c shows the image obtained by an adaptive-mesh GSP migration with this scheme. It corresponds well with the image obtained by the regular fixed-mesh GSP migration using the mesh with the grid interval $dx = dz = 6.25$ m (Fig. 13b), and the two interfaces can be easily imaged by both methods. In the second scheme, we apply the imaging condition to the single-frequency source wavefield and receiver wavefield, and then interpolate the single-frequency image afterwards. The final single-frequency image $I(x,z;\omega)$ on the common mesh can be expressed as

$$\begin{aligned} I(x,z;\omega) = {} & e_{11}[S_{11}(x_{11},z_{11};\omega) \times G_{11}(x_{11},z_{11};\omega)] + e_{12}[S_{12}(x_{12},z_{12};\omega) \\ & \times G_{12}(x_{12},z_{12};\omega)] + e_{21}[S_{21}(x_{21},z_{21};\omega) \times G_{21}(x_{21},z_{21};\omega)] \\ & + e_{22}[S_{22}(x_{22},z_{22};\omega) \times G_{22}(x_{22},z_{22};\omega)] + \ldots. \end{aligned} \tag{19}$$

As shown by red circles in Fig. 13, we find more artifacts in the image (Fig. 13d) obtained by this scheme compared with the fixed-mesh result (Fig. 13b) and the first scheme result (Fig. 13c). According to Eqs. (17) and (19), the first scheme retains more initial wavefield information than the second one such as the terms $S_{11}G_{12}$ and $S_{22}G_{11}$,which to some extent suppress the noise caused by mesh variation. Note that some artifacts in these three images are caused by the discrete Fourier transform in GSP and are independent of the applied method.

The second model we test is the Marmousi model shown in Fig. 14. The synthetic data were generated by the finite difference method with 8th order spatial accuracy and 2nd order temporal accuracy. The source is a Ricker wavelet with a dominant frequency of 25 Hz, a time shift of 0.05 s, and a record length of 3 s. The receivers are distributed on the surface from 0 m to 7437 m at an interval of 12.5 m, and the shot interval is 75 m. 144 frequencies have been used in both GSP

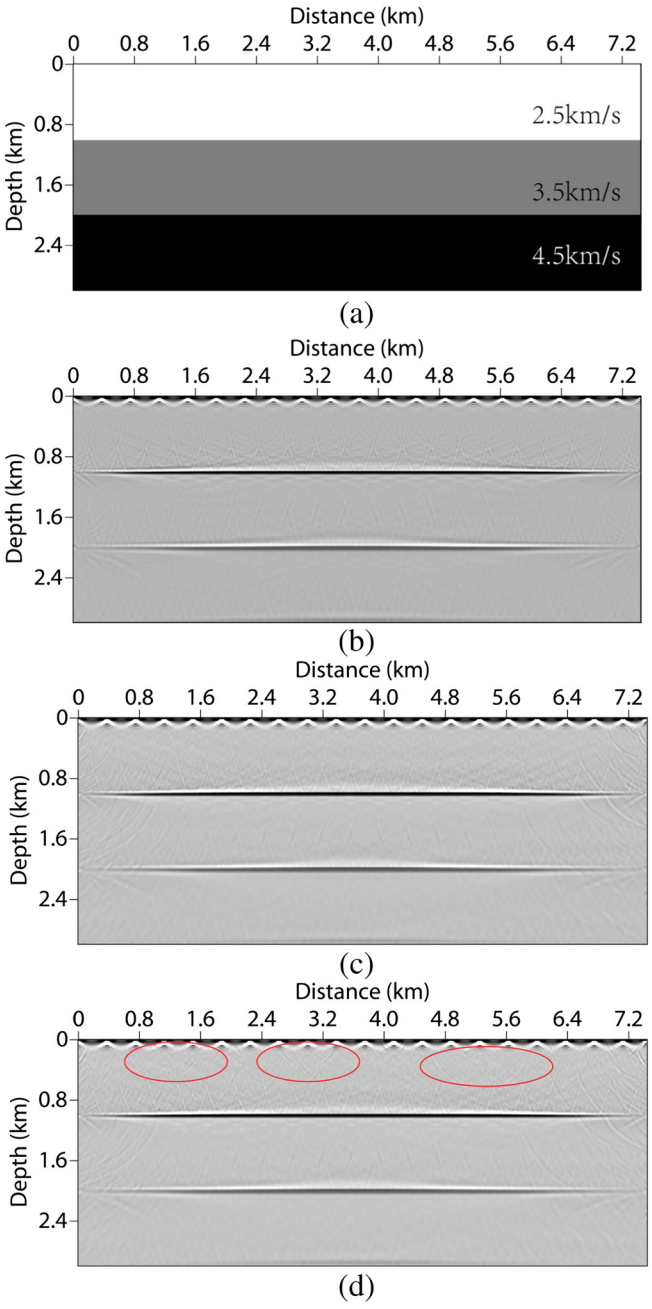

Fig. 13. Stacked images of the three-layer model with 20 shots. (a)A three-layer model; (b) Fixed-mesh GSP image; (c) Adaptive-mesh GSP image obtained by the first interpolation scheme; (d) Adaptive-mesh GSP image obtained by the second interpolation scheme. (For interpretation of the references to color in this figure legend, the reader is referred to the web version of this article.)

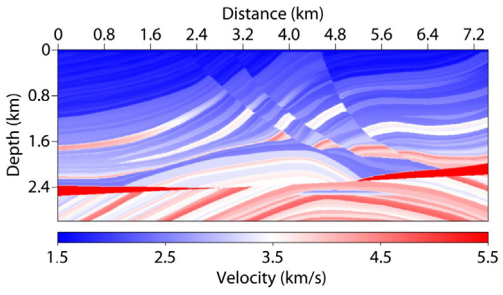

Fig. 14. Marmousi model. The length of the model is 7437 m and the depth is 2987 m. We discretize the model into 1191 × 479 grids with the grid interval $dx = dz = 6.25$ m.

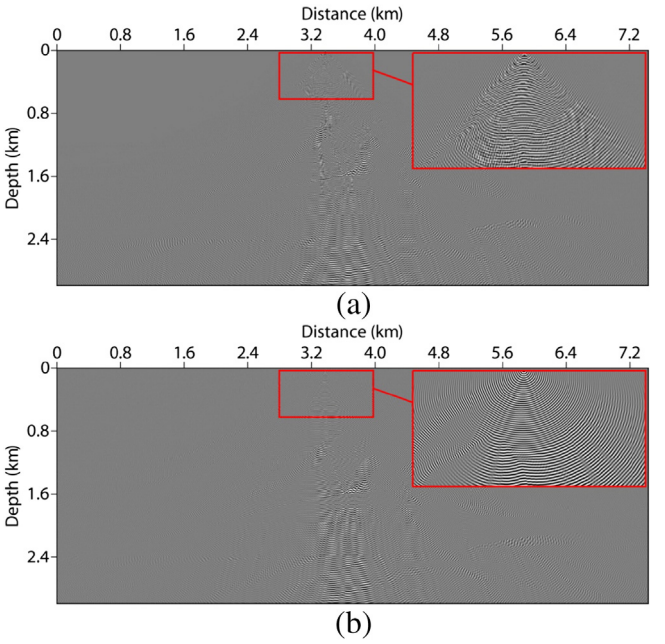

Fig. 15. The 150-Hz wavefields in the Marmousi model obtained by: (a) the fixed-mesh GSP using a mesh of 1191 × 479 grids with the grid interval $dx = dz = 6.25$ m; (b) the adaptive-mesh GSP using 7432 × 2989 grids with $dx = dz = 1.0$ m. The source location is (3375 m, 0). The red box is a zoom of the initial figure in small red box. (For interpretation of the references to color in this figure legend, the reader is referred to the web version of this article.)

methods with fixed mesh and adaptive mesh. The minimum frequency is 5 Hz and the maximum frequency is 40 Hz. To demonstrate the high performance of the frequency-adaptive meshes in modeling, a wavefield at 150 Hz (Fig. 15b) and a propagation angle at 2 Hz

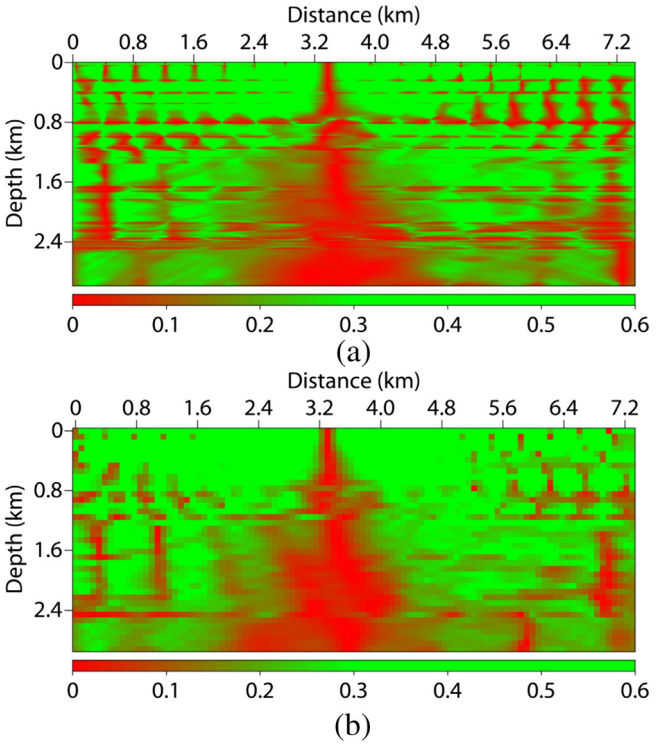

Fig. 16. Distributions of ray parameters for 2 Hz in the Marmousi model obtained by: (a) the fixed-mesh GSP using a mesh of 1191 × 479 grids with a grid interval $dx = dz = 6.25$ m; (b) the adaptive-mesh GSP using 96 × 39 grids with $dx = dz = 76.8$ m. The source location is (3375 m, 0).

(Fig. 16b) are shown, compared with the corresponding results from the fixed-mesh method (shown in Figs. 15a and 16a). Based on the enlarged image indicated by the big red box in Fig. 15, the adaptive-mesh method ensures accurate wavefields for the high frequency and improves the precision of propagation angles for the low frequency because the angle in Fig. 16b contains less 'knotted' anomalies than that in Fig. 16a. If a coarser mesh is used for the 2-Hz component, the accuracy of the propagation angle will increase further. For those methods using propagation angles such as the superwide-angle wave propagator, we can easily modify the mesh variation function $h(\omega)$ to make all meshes coarse enough so that the propagation angles are computed accurately and the wavefields satisfy the precision requirement simultaneously. Fig. 17 shows snapshots obtained by the fixed-mesh GSP and adaptive-mesh GSP. As the red arrows indicate, the frequency-adaptive mesh results in less numerical dispersion than the conventional single and fixed mesh.

Fig. 18a and b show the images generated by the regular GSP migration and the adaptive-mesh GSP migration, respectively. Compared with the image from the reverse time migration (Fig. 18c), these two methods limited by the one-way approximation also obtain a basic image of target areas: the three faults and the deep anticline. In particular, the image using adaptive meshes (Fig. 18b) contains fewer artifacts shown by red circles and as the arrow shows, the structures adjacent to the faults are better imaged than in the fixed-mesh one (Fig. 18a). In terms of efficiency, the computation cost is related to the choice of mesh variation function and the extra computation cost due to fine meshes demanded by high frequencies is generally balanced by the benefits at low frequencies. In fact, the efficiency of our approach may vary significantly for different frequency-domain propagators. In this numerical example, the adaptive-mesh GSP migration for a single-shot gather takes 33.2 s compared to 18.4 s for the fixed mesh migration on our computer. The implementation of GSP consists of many Fourier transforms switching the wavefield between the space domain and the wavenumber domain. As such, the computational time is higher than that of other propagators, although it is still acceptable. If the frequency band contains a small quantity of high frequencies, the computation time will decrease.

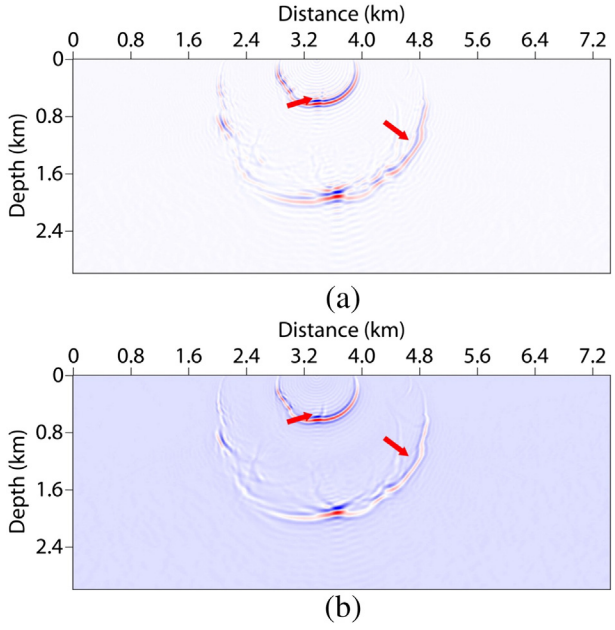

Fig. 17. Snapshots at 0.4 s and 0.9 s in the Marmousi model simulated by: (a) the fixed-mesh GSP using a mesh of 1191 × 479 grids with a grid interval $dx = dz = 6.25$ m, (b) the adaptive-mesh GSP using $h(f) = (v_{min}/f)/10$ as the mesh variation function. The source location is (3375 m, 0). (For interpretation of the references to color in this figure, the reader is referred to the web version of this article.)

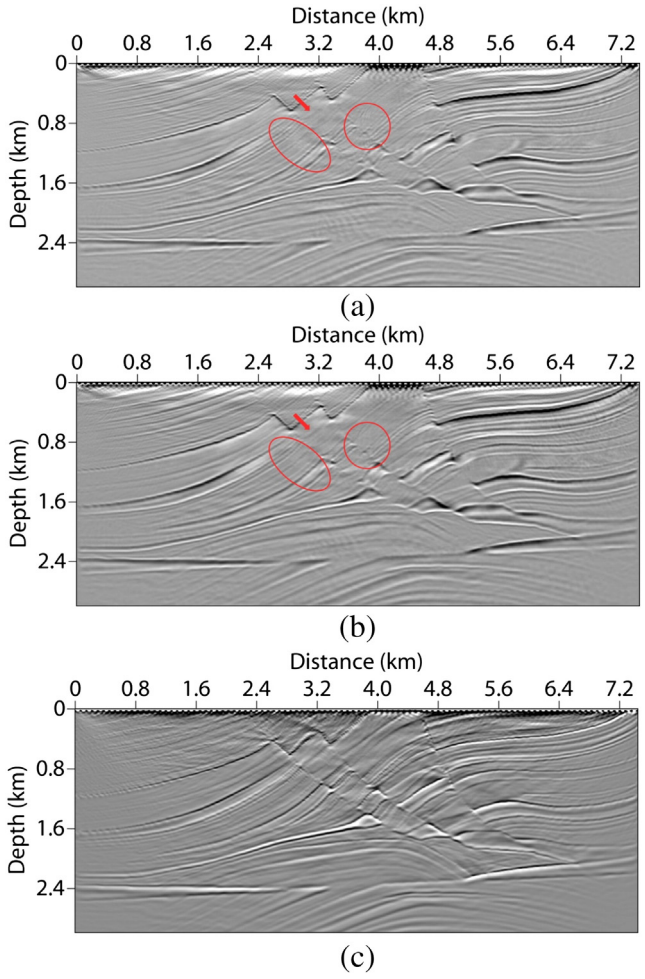

Fig. 18. Stacked images of the Marmousi model with 100 shots obtained by (a) Fixed-mesh GSP migration using the mesh of 1191 × 479 grids with $dx = dz = 6.25$ m; (b) adaptive-mesh GSP migration using $h(f) = (v_{min}/f)/10$; (c) reverse time migration.

4. Conclusions

We apply a numerical approach using frequency-adaptive meshes for seismic simulation in the frequency domain. This method automatically changes the mesh through the mesh variation function to meet the requirement of different frequencies. The mesh variation function is related to the frequency and is the key to applying this approach. Dispersion analysis indicates that it can be defined as the inversely proportional function and must be smooth in order to minimize the numerical dispersion. To apply this approach to modeling, two interpolations are required, i.e. interpolating velocity model and interpolating single-frequency wavefields onto a common mesh. The linear interpolation works well and cost less computational time. For migration, interpolating data traces using the parabolic function onto corresponding meshes is necessary.

In this study, we develop the theory of frequency-adaptive meshes for the Padé generalized screen propagator and do seismic modeling and migration test. Synthetic examples demonstrate that this adaptive-mesh method addresses two numerical modeling artifacts produced by fixed-grid spacing including the propagation angle anomalies of low-frequency wavefields and the numerical dispersion of high-frequency wavefields. And the modeling and migration results correspond well with the results obtained by regular methods. In terms of efficiency, the total cost increases in this test due to the way to do Fourier transforms compared with the fixed-grid method. However, the computational cost is acceptable allowing for the potential of the method

in propagation angle calculation, multi-scale study and frequency analysis. And it is quite easy to extend this approach to other frequency-domain methods such as the frequency domain finite difference. Furthermore, this scheme can be combined with space-dependent mesh, i.e., non-uniform mesh to address heterogeneous media more efficiently.

Acknowledgments

The authors are grateful to B. Chen, L.-X. Wen, J. Virieux and R.-E. Plessix for their fruitful discussions and suggestions. This study received support from the National Natural Science Foundation of China [grants 41374006 and 41274117]. This work is also supported by the Chinese Academy of Sciences and the State Administration of Foreign Experts Affairs International Partnership Program for Creative Research Teams.

Appendix A

This appendix gives a brief derivation of the Padé generalized screen propagator (GSP) (Xie and Wu, 1998). First, based on the perturbation theory, the medium velocity $v(x,z)$ can be divided into the constant reference v_0 and the variable perturbation velocity $\delta v(x,z) = v(x,z) - v_0$. Therefore, the 2D acoustic wave equation of the frequency-domain has the form of

$$\left(\frac{\partial^2}{\partial x^2} + \frac{\partial^2}{\partial z^2} + k_0^2 n^2\right) u(x,z) = 0, \tag{A.1}$$

where $u(x,z)$ is the frequency-domain wavefield; the $n = v_0/v(x,z)$ refers to the refraction index and $k_0 = \omega/v_0$is the reference wavenumber. From Eq. (A.1), we can write the downgoing wave equation as

$$\frac{\partial u(x,z)}{\partial z} = i\sqrt{n^2 k_0^2 + \frac{\partial^2}{\partial x^2}}\, u(x,z). \tag{A.2}$$

Under the small propagation angles approximation or for the media with small velocity perturbations, $\frac{\partial^2}{\partial x^2}$ is small. Hence the root square on the right hand side of Eq. (A.2) can be expanded by Taylor series. However, for the large velocity perturbations and wide angle situations, this expansion is no longer valid. An alternative is to use the Padé approximation which is

$$(1+x)^{1/2} = 1 + \cfrac{x/2}{1 + \cfrac{x/4}{1 + \cfrac{x/4}{1 + \cfrac{x/4}{\cdots}}}}. \tag{A.3}$$

Under the first-order Padé approximation of the square root function, Eq. (A.2) is modified as

$$\begin{aligned}\frac{\partial u(x,z)}{\partial z} &= ink_0 \left(1 + \frac{a\dfrac{1}{n^2k_0^2}\dfrac{\partial^2}{\partial x^2}}{1 + b\dfrac{1}{n^2k_0^2}\dfrac{\partial^2}{\partial x^2}}\right) u(x,z) \\ &= i\left(-\frac{\delta v(x,z)}{v(x,z)}k_0 + k_0 + \frac{nk_0 a\dfrac{1}{n^2k_0^2}\dfrac{\partial^2}{\partial x^2}}{1 + b\dfrac{1}{n^2k_0^2}\dfrac{\partial^2}{\partial x^2}}\right) u(x,z),\end{aligned} \tag{A.4}$$

in which a and b are expansion coefficients and $a = 1/2$, $b = 1/4$ for the first-order approximation. The wavefield $u(x,z)$ can be decomposed into a series of plane waves $u(k_x,z)e^{ik_x x}$, i.e.,

$$u(x,z) = \int u(k_x,z)e^{ik_x x}dk_x, \tag{A.5}$$

k_x is the horizontal wavenumber and it is related to the vertical wavenumber k_z as

$$k_z = \left(k_0^2 - k_x^2\right)^{1/2}. \tag{A.6}$$

After expanding the first-order Padé approximation, Eq. (A.6) has the form of

$$k_z = k_0\left(1 + \frac{a\zeta}{1+b\zeta}\right) \text{ or } k_0 = k_z - \frac{a\zeta}{1+b\zeta}k_0 \text{ with } \zeta = -k_x^2/k_0^2. \tag{A.7}$$

Substituting Eq. (A.7) into Eq. (A.4), we get

$$\frac{\partial u(x,z)}{\partial z} = i\left(-\frac{\delta v(x,z)}{v(x,z)}k_0 + k_z - \frac{a\zeta}{1+b\zeta}k_0 + \frac{nk_0 a\dfrac{1}{n^2k_0^2}\dfrac{\partial^2}{\partial x^2}}{1 + b\dfrac{1}{n^2k_0^2}\dfrac{\partial^2}{\partial x^2}}\right) u(x,z). \tag{A.8}$$

Considering Eq. (A.5), we perform the Fourier transform with respect to x on both sides of Eq. (A.8), and then

$$\frac{\partial u(k_x,z)}{\partial z} = i\left[k_z - k_0\left(\frac{\delta v(x,z)}{v(x,z)}*\right) + k_0\frac{a(n*)\eta}{1+b\eta} - k_0\frac{a\zeta}{1+b\zeta}\right] u(k_x,z), \tag{A.9}$$

where $\eta = -(1/n^{2*})(k_x^2/k_0^2)$; $(\delta v(x,z)/v(x,z)*)$, $(n*)$ and $(1/n^{2}*)$ are the Fourier transforms of $\delta v(x,z)/v(x,z)$, n and $1/n^2$ and "*" refers to the wavenumber domain convolution. Eq. (A.9) is already in the wavenumber domain. Combining the latter two terms and omitting high powers of k_x/k_0, we have

$$\frac{\partial u(k_x,z)}{\partial z} \approx i\left[k_z - k_0\left(\frac{\delta v(x,z)}{v(x,z)}*\right) - k_0\frac{a\left[\left(\dfrac{1}{n}*\right)-1\right]\dfrac{k_x^2}{k_0^2}}{1 - b\left[1 + \left(\dfrac{1}{n^2}*\right)\right]\dfrac{k_x^2}{k_0^2}}\right] u(k_x,z). \tag{A.10}$$

Both Eqs. (A.9) and (A.10) are downgoing wave equations with the first-order Padé approximation. However, Eq. (A.10) can be implemented more easily.

If the seismic wave propagates from z_0 to z_1 and $\Delta z = z_1 - z_0$ is small enough, we can neglect the vertical variation of n within Δz. Therefore, Eqs. (A.9) and (A.10) can be integrated with z. For the latter, omitting the term $b[1 + (1/n^{2}*)]k_x^2/k_0^2$ and integrating it with z, we can get

$$u(k_x,z_1) = \exp\left\{i\left[\Delta z k_z - \Delta z k_0\left(\frac{\delta v(x,z_0)}{v(x,z_0)}*\right) - \Delta z k_0 A\frac{k_x^2}{k_0^2}\right\}u(k_x,z_0), \tag{A.11}$$

where $A = (1/2)[(1/n^*) - 1]$. To improve the computational efficiency, the wavenumber domain convolution in Eq. (A.11) can be replaced by the space domain multiplication and under the approximation of

$$\exp\left\{-\Delta z k_0 A\frac{k_x^2}{k_0^2}\right\} = 1 - \Delta z k_0 A\frac{k_x^2}{k_0^2}, \tag{A.12}$$

we get the dual-domain expression of GSP for the first-order Padé

approximation as follows:

$$u(x,z_1)=\left(\mathrm{F}^{-1}-i\Delta z k_0 A\mathrm{F}^{-1}\frac{k_x^2}{k_0^2}\right)e^{i\Delta z k_z}\mathrm{F}e^{-i\Delta z k_0\frac{\delta v(x,z_0)}{v(x,z_0)}}u(x,z_0), \tag{A.13}$$

in which F denotes the Fourier transform from the space domain to the wavenumber domain while F^{-1} denotes the inverse Fourier transform from the wavenumber domain to the space domain. Moreover, if the larger velocity perturbations only exist in local regions, Eq. (A.13) can be modified to the space domain expression as

$$u(x,z_1)=\left[1+i\Delta z\frac{A}{k_0}\frac{\partial^2}{\partial x^2}\right]\times\mathrm{F}^{-1}e^{i\Delta z k_z}\mathrm{F}e^{-i\Delta z k_0\frac{\delta v(x,z_0)}{v(x,z_0)}}u(x,z_0). \tag{A.14}$$

On the right-hand side of Eqs. (A.13) and (A.14), the two exponential terms refer to the phase screen solution; the term in brackets is the modification for perturbations of large velocities and large angles.

References

Adriano, S., Oliveira, M., 2003. A fourth-order finite-difference method for the acoustic wave equation on irregular grids. Geophysics 68 (2), 1–5.

Aki, K., Richards, P., 1980. Quantitative Seismology: Theory and Methods. Freeman, San Francisco.

Alford, R.M., Kelly, K.R., Boore, D.M., 1974. Accuracy of finite-difference modelling of the acoustic wave equation. Geophysics 39 (6), 834–842.

Ansari, S., Farquharson, C.G., 2014. 3D finite-element forward modelling of electromagnetic data using vector and scalar potentials and unstructured grids. Geophysics 79 (4), E149–E165.

Aoi, S., Fujiwara, H., 1999. 3D finite-difference method using discontinuous grids. Bull. Seismol. Soc. Am. 89, 918–930.

Bansal, R., Sen, M.K., 2008. Finite-difference modelling of S-wave splitting in anisotropic media. Geophys. Prospect. 56, 293–312.

Bohlen, T., Saenger, E.H., 2006. Accuracy of heterogeneous staggered-grid finite-difference modelling of Rayleigh waves. Geophysics 71 (4), T109–T115.

Bruneton, M., Farra, V., Pedersen, H.A., the SVEKALAPKO Seismic Tomography Working Group, 2002. Non-linear surface wave phase velocity inversion based on ray theory. Geophys. J. Int. 151, 583–596.

Brzostowski, M.A., Black, J.L., 1989. Frequency dispersion in finite-difference migration. Geophysics 54 (11), 1435–1447.

Cerveny, V., 2001. Seismic Ray Theory. Cambridge University Press, Cambridge.

Chen, J., 2010. On the selection of reference velocities for split-step Fourier and generalized-screen migration methods. Geophysics 75 (6), S249–S257.

Chu, C., Stoffa, P.L., 2011. Application of normalized pseudo-Laplacian to elastic wave modelling on staggered grids. Geophysics 76 (5), T113–T121.

Dablain, M.A., 1986. The application of high-order differencing to the scalar wave equation. Geophysics 51 (1), 54–66.

Dickens, T.A., Winbow, G.A., 2011. RTM angle gathers using Poynting vectors. 81th Annual International Meeting, SEG, Expanded Abstracts, pp. 3109–3113.

Falk, J., Tessmer, E., Gajewski, D., 1998. Efficient finite-difference modelling of seismic waves using locally adjustable time step sizes. Geophys. Prospect. 46, 603–616.

Fan, N., Zhao, L., Gao, Y., Yao, Z., 2015. A discontinuous collocated-grid implementation for high-order finite-difference modelling. Geophysics 80 (4), T175–T181.

Fichtner, A., Trampert, J., Cupillard, P., Saygin, E., Taymaz, T., Capdeville, Y., Villaseñor, A., 2013. Multiscale full waveform inversion. Geophys. J. Int. 194 (1), 534–556.

Gosselin-Cliche, B., Giroux, B., 2014. 3D frequency-domain finite-difference viscoelastic-wave modelling using weighted average 27-point operators with optimal coefficients. Geophysics 79 (3), T169–T188.

Gray, S., 2006. Angle gathers for Gaussian beam depth migration. Proceedings of the 2006 CSPG, CSEG, CWLS Joint Convention, Expanded Abstracts, pp. 75–81.

Hayashi, K., Burns, D.R., 1999. Variable grid finite-difference modelling including surface topography. 69th Annual International Meeting, SEG, Expanded Abstracts, pp. 523–527.

Hicks, G.J., 2002. Arbitrary source and receiver positioning in finite-difference schemes using Kaiser windowed sinc functions. Geophysics 67 (1), P156–1166.

Hustedt, B., Operto, S., Virieux, J., 2004. Mixed-grid and staggered-grid finite-difference methods for frequency-domain acoustic wave modelling. Geophys. J. Int. 157, 1269–1296.

Jastram, C., Behle, A., 1992. Acoustic modelling on a grid of vertically varying spacing. Geophys. Prospect. 40, 157–169.

Jastram, C., Tessmer, E., 1994. Elastic modelling on a grid with vertically varying spacing. Geophys. Prospect. 42, 357–370.

Jia, X., Wu, R.-S., 2009a. Calculation of the wave propagation angle in complex media: application to turning wave simulations. Geophys. J. Int. 178, 1565–1573.

Jia, X., Wu, R.-S., 2009b. Superwide-angle one-way wave propagator and its application in imaging steep salt flanks. Geophysics 74 (4), S75–S83.

Jin, S., 2010. 5D seismic data regularization by a damped least-norm Fourier inversion. Geophysics 75 (6), WB103–WB111.

Kim, S., Cook, R., 1999. 3-D traveltime computation using second-order ENO scheme. Geophysics 64 (6), 1867–1876.

Krüger, O.S., Saenger, E.H., Shapiro, S.A., 2005. Scattering and diffraction by a single crack: An accuracy analysis of the rotated staggered grid. Geophys. J. Int. 162, 25–31.

Le Rousseau, J.H., de Hoop, M.V., 2001a. Modeling and imaging with the scalar generalized-screen algorithms in isotropic media. Geophysics 66 (5), P1551–P1568.

Le Rousseau, J.H., de Hoop, M.V., 2001b. Scalar generalized-screen algorithms in transversely isotropic media with a vertical symmetry axis. Geophysics 66 (5), P1538–P1550.

Li, Y., Métivier, L., Brossier, R., Han, B., Virieux, J., 2015. 2D and 3D frequency-domain elastic wave modelling in complex media with a parallel iterative solver. Geophysics 80 (3), T101–T118.

Liu, Y., Sen, M.K., 2011a. Finite-difference modelling with variable length spatial operators and time steps. 81st Annual International Meeting, SEG, Expanded Abstracts, pp. 2834–2838.

Liu, Y., Sen, M.K., 2011b. Finite-difference modelling with adaptive variable-length spatial operators. Geophysics 76 (4), T79–T89.

Martin, B., Fornberg, B., St-Cyr, A., 2015. Seismic modelling with radial-basis-function-generated finite differences. Geophysics 80 (4), T137–T146.

Moczo, P., 1989. Finite-difference technique for SH-waves in 2-D media using irregular grids-application to the seismic response problem. Geophys. J. Int. 99, 321–329.

Moreira, R.M., Cetale Santos, M.A., Martins, J.L., Silva, D.L.F., Pessolani, R.B.V., Filho, D.M.S., Bulcão, A., 2014. Frequency-domain acoustic-wave modelling with hybrid absorbing boundary conditions. Geophysics 79 (5), A39–A44.

Operto, S., Virieux, J., Amestoy, P., L'Excellent, J.-Y., Giraud, L., Ben-Hadj-Ali, H., 2007. 3D finite-difference frequency-domain modeling of visco-acoustic wave propagation using a massively parallel direct solver: a feasibility study. Geophysics 72 (5), SM185–SM211.

Operto, S., Brossier, R., Combe, L., Métivier, L., Ribodetti, A., Virieux, J., 2014. Computationally efficient three-dimensional acoustic finite-difference frequency-domain seismic modelling in vertical transversely isotropic media with sparse direct solver. Geophysics 79 (5), T257–T275.

Opršal, I., Zahradník, J., 1999. Elastic finite-difference method for irregular grids. Geophysics 64 (1), 240–250.

Pratt, R.G., Worthington, M.H., 1990. Inverse theory applied to multi-source cross-hole tomography. Part 1: acoustic wave- equation method. Geophys. Prospect. 38, 287–310.

Qian, J., Symes, W.W., 2002. An adaptive finite-difference method for traveltimes and amplitudes. Geophysics 67 (1), 167–176.

Qian, J., Zhang, Y.T., Zhao, H.K., 2007. A fast sweeping method for static convex Hamilton–Jacobi equations. J. Sci. Comput. 31 (1), 237–271.

Qin, F., Luo, Y., Olsen, K.B., Cai, W., Schuster, G.T., 1992. Finite-difference solution of the eikonal equation along expanding wavefronts. Geophysics 57 (3), 478–487.

Ren, Z., Liu, Y., 2015. Acoustic and elastic modelling by optimal time–space-domain staggered-grid finite-difference schemes. Geophysics 80 (1), T17–T40.

Ruud, B.O., 2006. Ambiguous reflection coefficients for an elastic media. Stud. Geophys. Geod. 50, 479–498.

Saenger, E.H., Gold, N., Shapiro, S.A., 2000. Modelling the propagation of elastic waves using a modified finite-difference grid. Wave Motion 31, 77–92.

Sava, P., Fomel, S., 2003. Angle-domain common-image gathers by wavefield continuation methods. Geophysics 68 (3), 1065–1074.

Shan, G., 2009. Optimized implicit finite-difference and Fourier finite-difference migration for VTI media. Geophysics 74 (6), WCA189–WCA197.

Shin, S., Byun, J., Seol, S.J., 2015. Imaging tilted transversely isotropic media with a generalised screen propagator. Explor. Geophys. 46, 349–358.

Sun, J., Yang, H., Han, F., 2007. A finite difference scheme for solving the eikonal equation with varying grid spacing. 77th Annual International Meeting, SEG, Expanded Abstracts, pp. 2120–2124.

Sun, W., Zhou, B., Fu, L.-Y., 2010. Dip angle-compensated one-way wave equation migration. Explor. Geophys. 41, 137–145.

Sun, J., Sun, Z., Han, F., 2011. A finite difference scheme for solving the eikonal equation including surface topography. Geophysics 76 (4), T53–T63.

Tessmer, E., 2000. Seismic finite-difference modelling with spatially varying time steps. Geophysics 65 (4), 1290–1293.

Ursin, B., de Hoop, M.V., Brandsberg-Dahl, S., Sollid, A., 2005. Seismic angle migration. Lead. Edge 24, 637–640.

Vidale, J., 1988. Finite-difference calculation of travel times. Bull. Seismol. Soc. Am. 78 (6), 2062–2076.

Wang, Y., Schuster, G.T., 1996. Finite-difference variable grid scheme for acoustic and elastic wave equation modelling. 66th Annual International Meeting, SEG, Expanded Abstracts, pp. 674–677.

Wang, H., Tao, G., Zhang, K., 2013. Wavefield simulation and analysis with the finite-element method for acoustic logging while drilling in horizontal and deviated wells. Geophysics 78 (6), D525–D543.

Wang, Y., Liang, W., Nashed, Z., Li, X., Liang, G., Yang, C., 2014. Seismic modelling by optimizing regularized staggered-grid finite-difference operators using a time–space-domain dispersion-relationship-preserving method. Geophysics 79 (5), T277–T285.

Xie, X., Wu, R.-S., 1998. Improve the wide angle accuracy of screen method under large contrast. 68th Annual International Meeting, SEG, Expanded Abstracts, pp. 1811–1814.

Zhang, W., Chen, X., 2006. Traction image method for irregular free surface boundaries in finite difference seismic wave simulation. Geophys. J. Int. 167, 337–353.

Zhao, H., 2005. A fast sweeping method for eikonal equations. Math. Comput. 74 (250), 603–627.